ARTICLE

Synthesis of Ultrahigh-Purity (6,5) Carbon Nanotubes Using a Trimetallic Catalyst

Satoru Shiina,◆ Tennpei Murohashi,◆ Koyo Ishibashi, Xing He, Takashi Koretsune, Zheng Liu, Wataru Terashima, Yuichiro K. Kato, Kazutoshi Inoue, Mitsuhiro Saito, Yuichi Ikuhara, and Toshiaki Kato*

Read Online

ACCESS | Metrics & More | Article Recommendations | Supporting Information

ABSTRACT: Chirality-controlled synthesis of carbon nanotubes (CNTs) is one of the ultimate goals in the field of nanotube synthesis. At present, direct synthesis achieving a purity of over 90%, which can be called single-chirality synthesis, has been achieved for only two types of chiralities: (14,4) and (12,6) CNTs. Here, we realized an ultrahigh-purity ($\sim$95.8%) synthesis of (6,5) CNTs with a trimetallic catalyst NiSnFe. Partial formation of Ni_3Sn crystals was found within the NiSnFe nanoparticles. The activation energy for the selective growth of (6,5) CNTs decreased owing to the formation of Ni_3Sn crystals, resulting in the high-purity synthesis of (6,5) CNTs. Transmission electron microscopy (TEM) reveals that one-dimensional (1D) crystals of periodic strip lines with 8.8 Å spacing are formed within the as-grown ultrahigh-purity (6,5) CNTs, which are well-matched with the simulated TEM image of closely packed 37 (6,5) CNTs with 2.8 Å intertube distance, indicating the direct formation of chirality-pure (6,5)-CNT bundle structures. The photoluminescence (PL) lifetime increases more than 20 times by the formation of chirality-pure bundle structures of (6,5) CNTs compared to that of isolated (6,5) CNTs. This can be explained by exciton delocalization or intertube excitons within bundle structures of chirality-pure (6,5) CNTs.

KEYWORDS: carbon nanotubes, single-chirality synthesis, trimetallic catalyst, chirality-pure bundle, plasma CVD
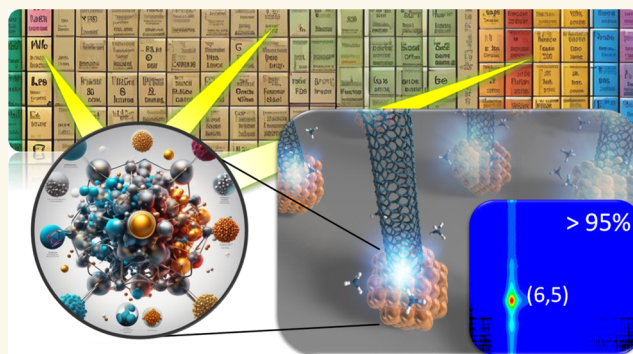
INTRODUCTION

Chirality-controlled synthesis of single-walled carbon nanotubes (SWNTs) is one of the most sought-after goals in the field of carbon nanotube (CNT) synthesis. To date, nearly single-chirality synthesis (over 90% purity) has been realized only for two kinds of chiralities among over 180 types of SWNTs, 97% (14,4) CNT with W_6Co_7,[11] 92% (12,6) CNT with W_6Co_7,[22] and 90% (12,6) CNT with the Mo_2C catalyst.[3] (14,4) CNT is the only semiconductor SWNT (s-SWNT) that realized over 90% purity synthesis, but has a narrow band gap (BG) ($\sim$0.63 eV) and low photoluminescence quantum yield (QYPL). As small diameter (d) ($<\sim$1 nm) s-SWNTs possess a wider band gap ($>\sim$1 eV) and higher QYPL, small diameter s-SWNTs are prime targets for single-chirality synthesis in optoelectronic and biological applications.

Over the past few decades, multiple methods have been explored for the chirality-controlled synthesis of SWNTs. In addition to the near-single-chirality synthesis (>90%) discussed above,[1−3] preferential syntheses (50−80% purity) have been reported for (8,4) CNTs (80% purity),[3] (10,9) CNTs (80% purity),[4] (16,0) CNTs (79.2% purity),[5] (12,6) CNTs (70% purity),[6] (9,8) CNTs (59.1% purity),[7] (6,5) CNTs (51−67% purity),[8−11] and (6,4) CNTs (57% purity)[12] (Figure 1). Predominant growth (30−50%) has also been reported for various catalysts.[13,14] For chemical vapor deposition (CVD) growth of SWNTs, only elemental or bimetallic catalysts for a total of approximately 14 catalysts have been investigated, comprising only 0.5% of all possible bimetallic combinations (Table S1 and Figure S1).[13,14] Inspired by the various alloys and intermetallic compounds reported for hydrogen storage ($LaNi_5$),[15] superconductors (MgB_2),[16] shape memory (TiNi),[17] and CO_2 reforming catalysts (Ni_5Ga_3),[18] it can be conjectured that a large space of possible materials can be
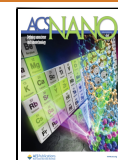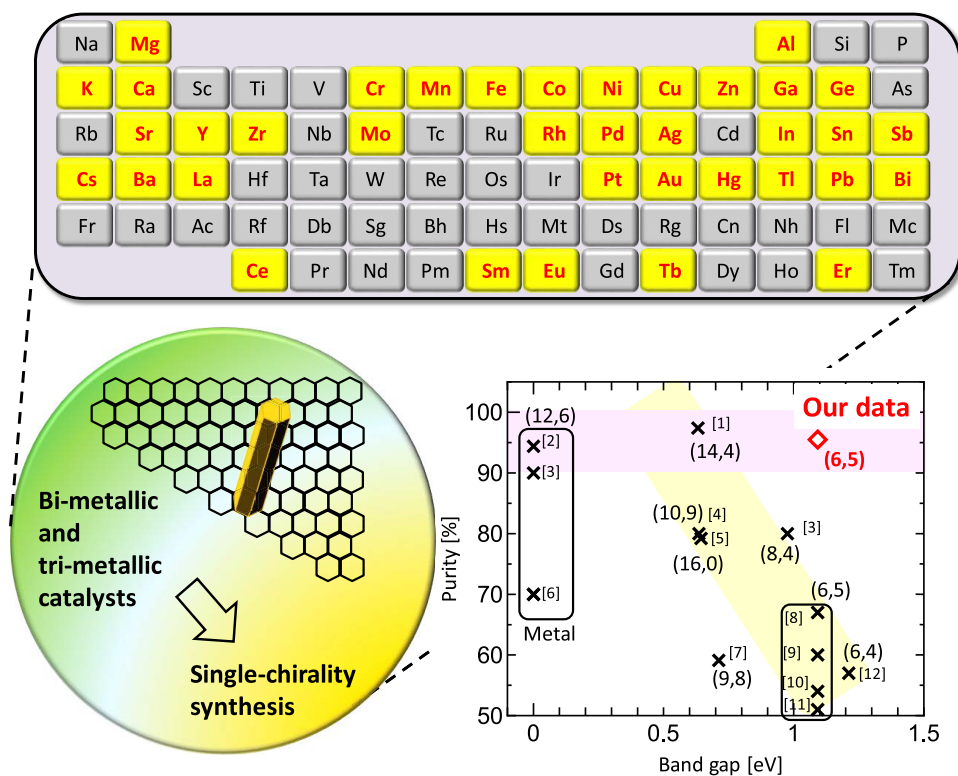
Figure 1. Basic concept of formation of ultrahigh-purity (6,5) CNT from the trimetallic catalyst.

explored for the single-chirality synthesis of SWNTs with various bimetallic, trimetallic, or even more complex catalysts that have not been systematically investigated to date.

In this study, we have realized an ultrahigh-purity (~95.8%) synthesis of (6,5) CNTs with a trimetallic catalyst. Systematic investigations of a total of 59 catalysts (41 bimetallic and 18 trimetallic) reveal that the NiSnFe catalyst acts as a special catalyst for the near-single-chirality synthesis of (6,5) CNTs. Partial formation of Ni_3Sn crystals was observed within the NiSnFe nanoparticles. The activation energy for the selective growth of (6,5) CNTs decreased owing to the formation of Ni_3Sn crystals, resulting in a high-purity synthesis of (6,5) CNTs. Furthermore, transmission electron microscopy (TEM) analysis revealed that outstanding bundle structures are formed within as-grown (6,5) CNTs. Periodically aligned lattice structures with a spacing of 8.8 Å are formed, matching well the simulated TEM image of the 37-(6,5) CNT bundle with an intertube distance of 0.28 nm, indicating that chirality-pure (6,5) CNT bundle structures should be directly fabricated using high-purity as-grown (6,5) CNTs. The photolumines-cence (PL) lifetime of (6,5)-CNT bundle structures increases more than 20 times by the formation of bundle structures of (6,5) CNTs compared to that of isolated (6,5) CNTs, indicating that hybridization of the electron wave functions of the individual (6,5) CNTs occurs in the (6,5) CNT bundle structures, giving rise to excitonic interactions such as exciton delocalization or intertube exciton formation.

RESULTS AND DISCUSSION

Trimetallic Catalyst. The effects of various kinds of catalysts on the chirality selectivity were systematically investigated using a step-by-step approach. First, we selected Ni as the main catalyst and added various metals (Ag, Al, Au, Ba, Bi, Ca, Ce, Cl, Co, Cr, Cs, Cu, Er, Eu, Fe, Ga, Ge, Hg, I, In,

K, La, Li, Lu, Mg, Mn, Mo, Pb, Pd, Pt, Rh, Sm, Sn, Sr, Tb, Te, Tl, Y, Yb, Zn, and Zr) to form 41 different bimetallic catalysts, followed by the growth of SWNTs under the same conditions (Figure 1). For all bimetallic catalysts, the chirality distribution was measured by using photoluminescence−excitation (PLE) mapping. Surprisingly, NiSn showed very high purity for (6,5) CNTs (Figures 2a and S2). Next, the third element was added to NiSn to form trimetallic catalysts. Interestingly, the PL intensity increased by more than six times after the addition of Fe to NiSn while maintaining a high purity of (6,5) CNTs (Figures 2b and S3). Further adjustment of the growth conditions (discussed in later sections) enabled the ultrahigh-purity (>95%) synthesis of (6,5) CNTs as estimated by PLE mapping (estimated purity of ~95.2%) (Figures 2c and S4) and UV−vis−near-infrared (NIR) spectroscopy (estimated purity of ~95.8%) (Figures 2d−f and S5 and Table S2). Radial breathing mode (RBM) analysis was also performed by using Raman scattering spectroscopy with multiple excitation laser wavelengths. For excitation at 532 nm, a single RBM peak was observed at 303 cm^{-1} (assigned as (6,5) with the Kataura plot) from 886 spots (Figures 2g and S6 and Table S3). Forty peaks were observed at 287 cm^{-1} (assigned as (7,5)) for the same number of 886 spots with 633 nm excitation. Other laser excitations at 442 and 785 nm did not show the RBM peak from the 886 and 243 spots, respectively, indicating that the obtained (6,5) CNT sample is approximately 93.8% pure, which is quite close to the purity values estimated with the PL and UV−vis−NIR spectroscopy techniques (Figure S6 and Table S3). Although the RBM peaks exhibit slight shifts depending on their location (inset in Figure 2g), all RBM peaks are distributed with a Raman shift difference of $\Delta\omega = 2.7$ cm^{-1} (Figure S6d,e). This 2.7 cm^{-1} difference is not attributed to the presence of other chirality components (Figure S6b), but it is likely dependent on the state of existence of (6,5)
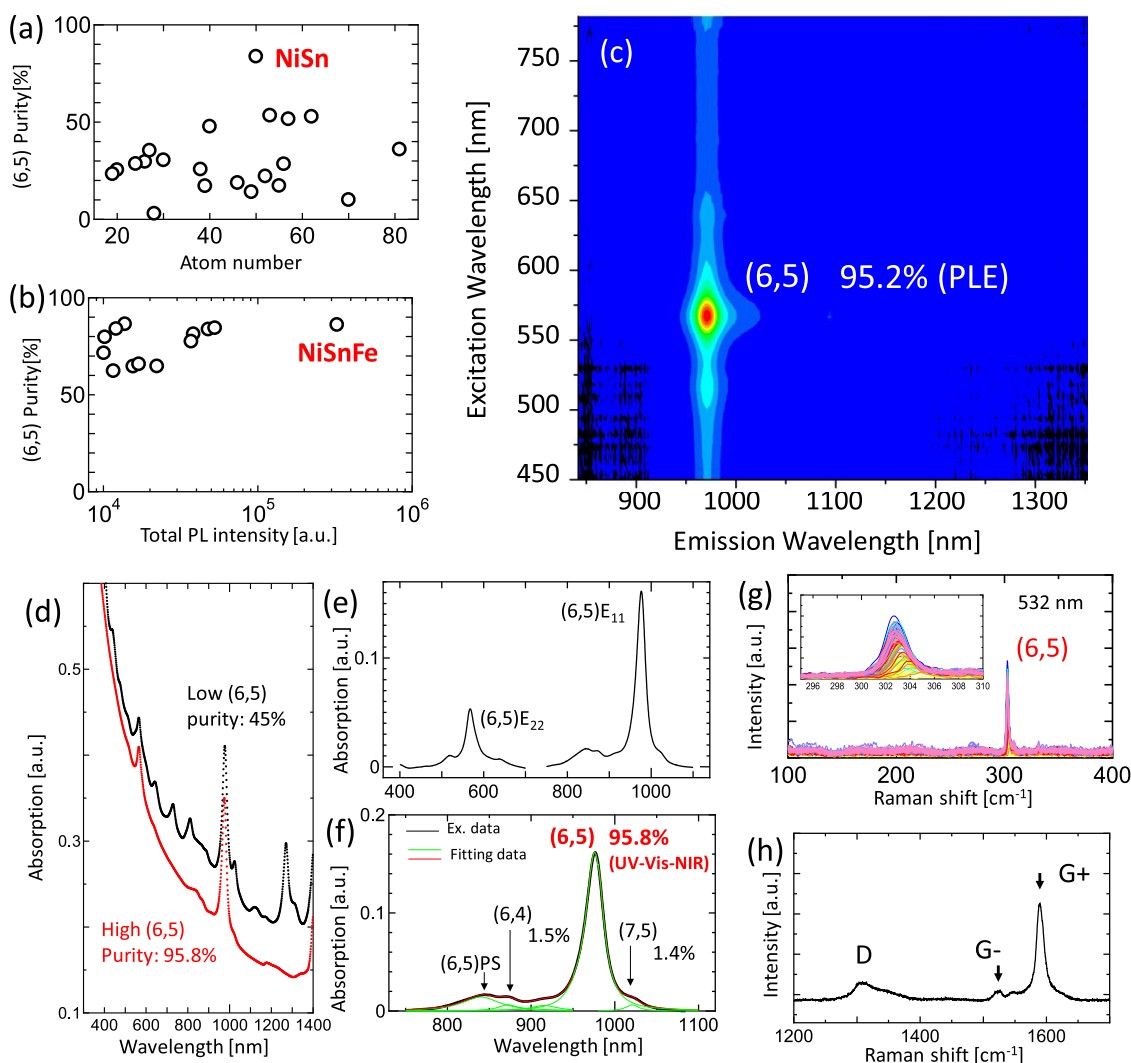
Figure 2. Ultrahigh-purity synthesis of (6,5) CNTs. (a) (6,5) CNT purity as a function of the atomic number of the element used for the bimetallic catalyst. (b) Purity vs total PL intensity of (6,5) CNTs grown from various trimetallic catalysts. (c) PLE mapping of ultrahigh-purity (6,5) CNTs grown from the NiSnFe catalyst. (d) Wide-range raw UV−vis−NIR spectra for (red) ultrahigh-purity and (black) low-purity (6,5) CNTs. Base-subtracted UV−vis−NIR spectra for (e) wide and (f) narrow wavelength range of ultrahigh-purity (6,5) CNTs. (g) RBM, (h) D and G bands of Raman scattering spectra of ultrahigh-purity (6,5) CNTs grown from the NiSnFe catalyst. The inset in (f) shows the enlarged spectra of (6,5) CNT peaks.

CNTs, such as a mixture of isolated and bundled states. The peak positions of the G+ (1589.2 cm^{-1}) and G− (1527 cm^{-1}) bands in the Raman spectra (Figure 2h), as well as the E11, E22, and E33 (Figure S5b) bands, and the phonon sideband (PS) in the UV−vis−NIR spectra (Figure 2f and Table S2) match well the chemically separated high purity (98%) of (6,5) CNTs, indicating that the estimated purity is reliable.[19] Although a slightly elevated D-peak is observable in our (6,5) CNTs (Figure 2h), a distinct tubular structure with a straight graphitic wall is apparent in the TEM images (Figure S7). This indicates that the origin of the D-peak is not attributable to the suboptimal crystal structure of our CNTs but rather to byproducts, such as amorphous carbon and materials resembling carbon nanowalls. Field-effect transistors (FET) were also fabricated with the obtained ultrahigh-purity (6,5) CNTs and demonstrated a high on/off ratio (>10^4) of the source−drain current (I_{ds}) and a wide off-state gate bias (V_g) region (>80 V) under various drain−source bias voltages

(V_{ds}), indicating a wider band gap of the (6,5) CNTs (Figure S8). The nonlinearity of $I_{ds} − V_{ds}$ indicates that ohmic contacts are not established, which is a characteristic often observed in CNT-FETs with diameters below 1 nm with Au electrodes.[20] These results indicate that our ultrahigh-purity (6,5) CNTs can be useful for various optoelectronic applications.

Growth Mechanism of (6,5) CNTs. Further investigations were carried out to reveal the mechanism of the ultrahigh-purity synthesis of (6,5) CNTs. X-ray absorption near edge structure (XANES) and extended X-ray absorption fine structure (EAXFS) analysis showed that the Ni component changed from pure Ni to NiO upon the addition of Sn and Fe (Figures 3a,b and S9). X-ray diffraction (XRD) spectra revealed that Ni$_3$Sn crystals were formed in both NiSn and NiSnFe where ultrahigh-purity (6,5) CNTs were grown (Figure 3c,d). Furthermore, the Ni$_3$Sn peak intensity drastically increased from NiSn to NiSnFe, along with the (6,5) CNT yield (Figure 3e−g). These results indicate that
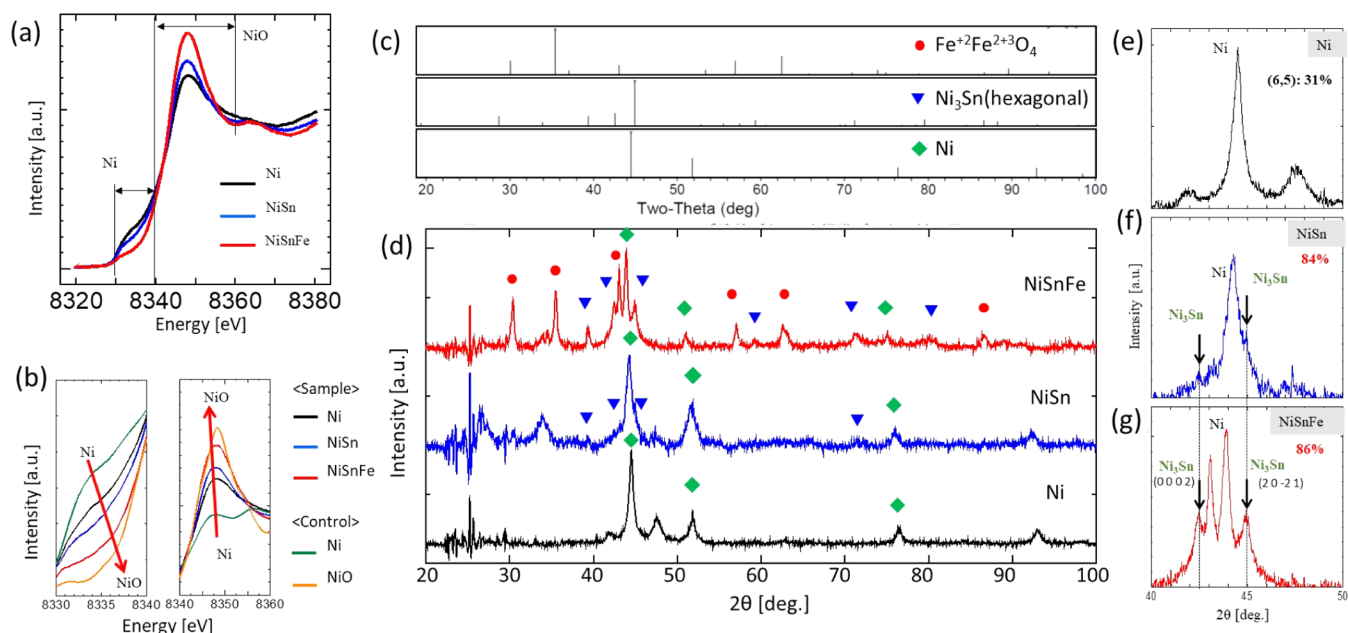
Figure 3. Detailed analysis of the NiSnFe catalyst with XANES and XRD after the plasma CVD. (a) Wide and (b) narrow energy range of XANES spectra of Ni, NiSn, and NiSnFe with the control data of Ni and NiO. (c) Calculated peak positions of Ni, Ni_3Sn, $Fe^{2+}Fe^{2+3}O_4$ in XRD spectra. (d) XRD spectra of Ni, NiSn, and NiSnFe. Enlarged XRD spectra of (e) Ni, (f) NiSn, and (g) NiSnFe, where (6,5) CNT purity was 31, 84, and 86%, respectively. To enhance the signal intensity during XRD measurements, the concentration of NiSnFe was increased from the usual 0.5 to 10 wt % for the experiment. It should be noted that the (6,5) CNT purity shown is based on the synthesis results obtained from the 10 wt % catalyst used for XRD measurements.
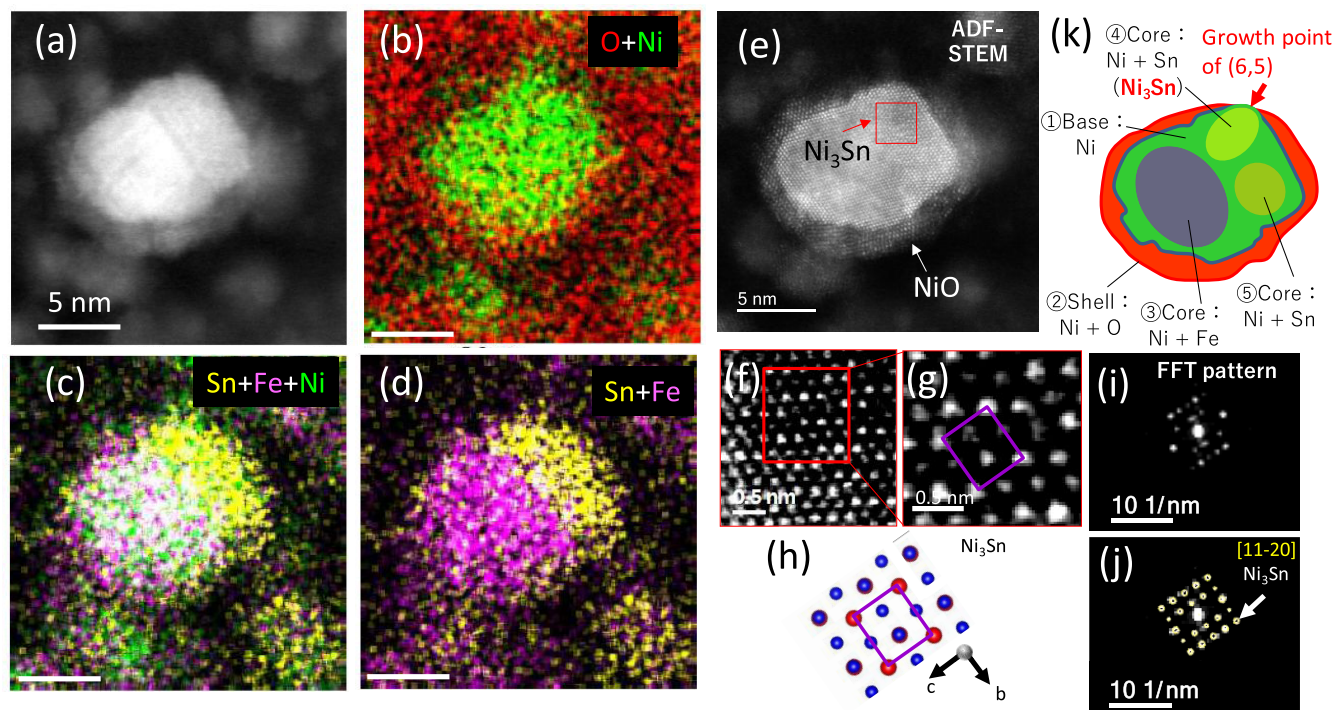

Figure 4. Detailed analysis of the NiSnFe catalyst with STEM after the plasma CVD. (a) Annular dark-field (ADF)-STEM, overlapped EDX mapping image for (b) O + Ni, (c) Sn + Fe + Ni, (d) Sn + Fe of NiSnFe nanoparticle used for (6,5) CNT growth. ADF-STEM image of (e) whole NiSnFe nanoparticle and specific (f, g) core region assigned as Ni_3Sn. (f) Middle and (g) high-magnification ADF-STEM images, and (h) possible atomic structures of Ni_3Sn. (i) The fast Fourier transform (FFT) pattern and (j) the simulated FFT pattern of Ni_3Sn overlapped with (i). (k) A detailed structural image of the NiSnFe nanoparticle revealed in the STEM measurements.

Ni_3Sn is a potential candidate for the selective growth of (6,5) CNTs. Further direct measurements were performed using scanning transmission electron microscopy (STEM). The catalysts contributing to CNT growth are nanoparticles smaller than 5 nm in size. However, accurately identifying the structure of completely unknown ternary system nanoparticles smaller
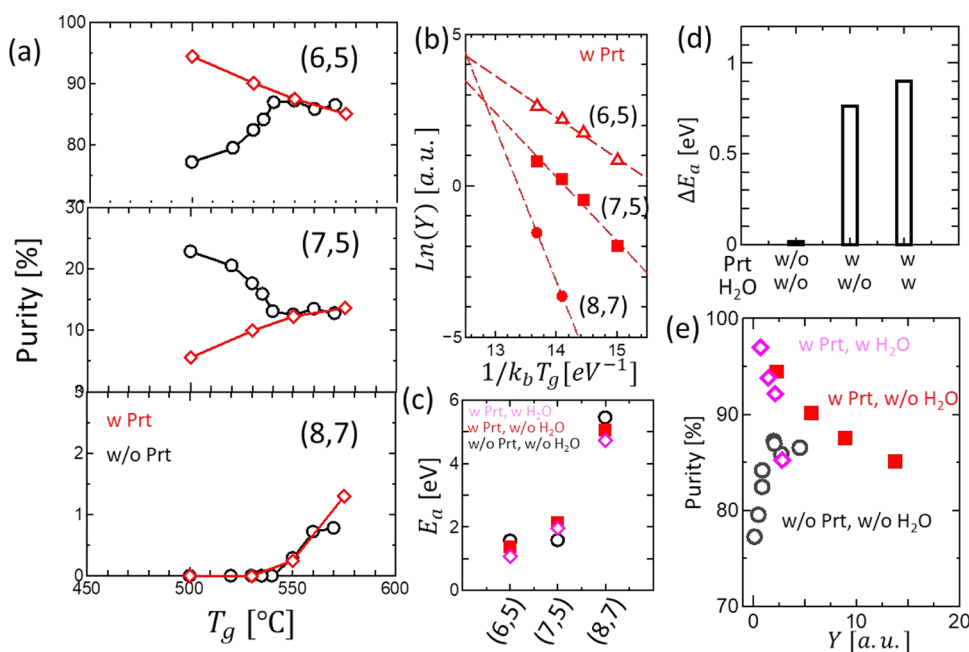
Figure 5. (a) Purity of (6,5), (7,5), and (8,7) CNTs as functions of T_g and with or without P_{rt}. (b) Arrhenius plots of each chirality Y grown with P_{rt}, where k_b is the Boltzmann constant. (c) E_a of (6,5), (7,5), and (8,7) CNTs grown under different conditions ($\diamond$: with P_{rt} and with H_2O, $\blacksquare$: with P_{rt} and without H_2O, $\circ$: without P_{rt} and without H_2O). (d) ΔE_a with and without P_{rt} and H_2O. (e) Purity vs Y of (6,5) CNTs grown under the different conditions ($\diamond$: with P_{rt} and with H_2O, $\blacksquare$: with P_{rt} and without H_2O, $\circ$: without P_{rt} and without H_2O).

than 5 nm is challenging. Therefore, we first conducted a detailed analysis of the composition and structure of relatively larger, structurally stable nanoparticles (~20 nm) that are less susceptible to electron beam damage. The STEM images and energy-dispersive X-ray (EDX) mappings revealed that the catalyst particles tend to form core–shell-like structures (Figures 4a–d and S10). The core of the Ni-based particles was covered by a NiO shell (Figure 4b,k). Furthermore, Fe and Sn were isolated within the Ni-core region (Figures 4c,d and S11). STEM measurements revealed that a part of the Ni + Sn region in the core formed Ni₃Sn crystals (Figures 4e–j, S12, and S13). The detailed identification of the Ni₃Sn crystal structure is shown in Figure S13. The thickness of the NiO shell appears thinner around the Ni₃Sn surface compared to other structures (Figures 4e and S14). While it is challenging to determine whether the NiO shell is formed before or after CNT growth, it is conceivable that the relatively strong reduction effects on the Ni₃Sn surface may impede oxidation, leading to the formation of misaligned core and shell centers or partially opened core–shell structures (Figure S10). These results are consistent with the XRD results and indicate that Ni₃Sn is predominantly responsible for the ultrahigh-purity synthesis of (6,5) CNTs. Therefore, having predicted the possible structures of NiSnFe nanoparticles, measurements were conducted on nanoparticles smaller than 5 nm that actually contribute to the growth of CNTs. Similar structures, including the isolation of Fe and Sn within core–shell structures and the formation of Ni₃Sn within Ni + Sn cores, have also been observed in small NiSnFe nanoparticles (<5 nm) (Figures S15 and S16). This indicates that Ni₃Sn directly facilitates the growth of (6,5) CNTs (Figures S15 and S16). The observed partially opened Ni₃Sn cores exhibit (0001) planes (Figure S16), suggesting that the degree of oxidation may strongly depend on the plane of Ni₃Sn, and only (0001) Ni₃Sn prevents oxidation, leading to the selective growth of

(6,5) CNTs. While direct evidence for why only specific facets of Ni₃Sn are exposed from the NiO shell could not be provided in this study, a similar phenomenon of growth rate variation depending on crystal planes has been widely reported in other crystals as well. Factors such as interfacial atomic density, interfacial matching, chemical bonding, temperature, thermodynamic parameters, and polarity have been reported to influence the growth rate of films.[21,22] Further detailed elucidation of the atomic structure of the NiSnFe catalyst surface remains a potential future subject of this study.

The plot of purity vs absolute PL intensity of (6,5) CNTs grown with various concentrations of Ni, Sn, and Fe reveals that the purity and yield of (6,5) CNTs are sensitive to the concentrations of Sn and Fe (Figure S17), respectively, indicating that the formation of Ni₃Sn is critical for increasing the purity of (6,5) CNTs, and that Fe assists in enhancing the formation of Ni₃Sn within the Ni-core region owing to the low solubility of Fe and Sn.

Systematic investigations were also carried out to determine the mechanism of the ultrahigh-purity synthesis of (6,5) CNTs. The purity of (6,5) CNTs gradually increased with decreasing growth temperature (T_g) (Figure 5a). This tendency was observed only when preheating (P_{rt}) was performed at 550 °C for 2 min immediately prior to the synthesis. The XRD spectra indicate that a distinct Ni₃Sn peak becomes evident only when the NiSnFe catalyst is heated to temperatures exceeding 550 °C (Figure S18). This indicates that the formation of Ni₃Sn should be enhanced during the P_{rt}. The activation energies (E_a) for the growth of these chiralities were estimated from the Arrhenius plot of the (n,m) yield (Y) that was estimated from the absolute (n,m) peak area of the UV–vis–NIR spectra (Figure 5b), showing that the E_a values for (6,5) CNTs (E_{a65}) and (7,5) CNTs (E_{a75}) were almost the same and were both lower than that of (8,7) CNTs (E_{a87}) without P_{rt} (Figure 5c). After P_{rt}, E_{a65} and E_{a75} decrease and
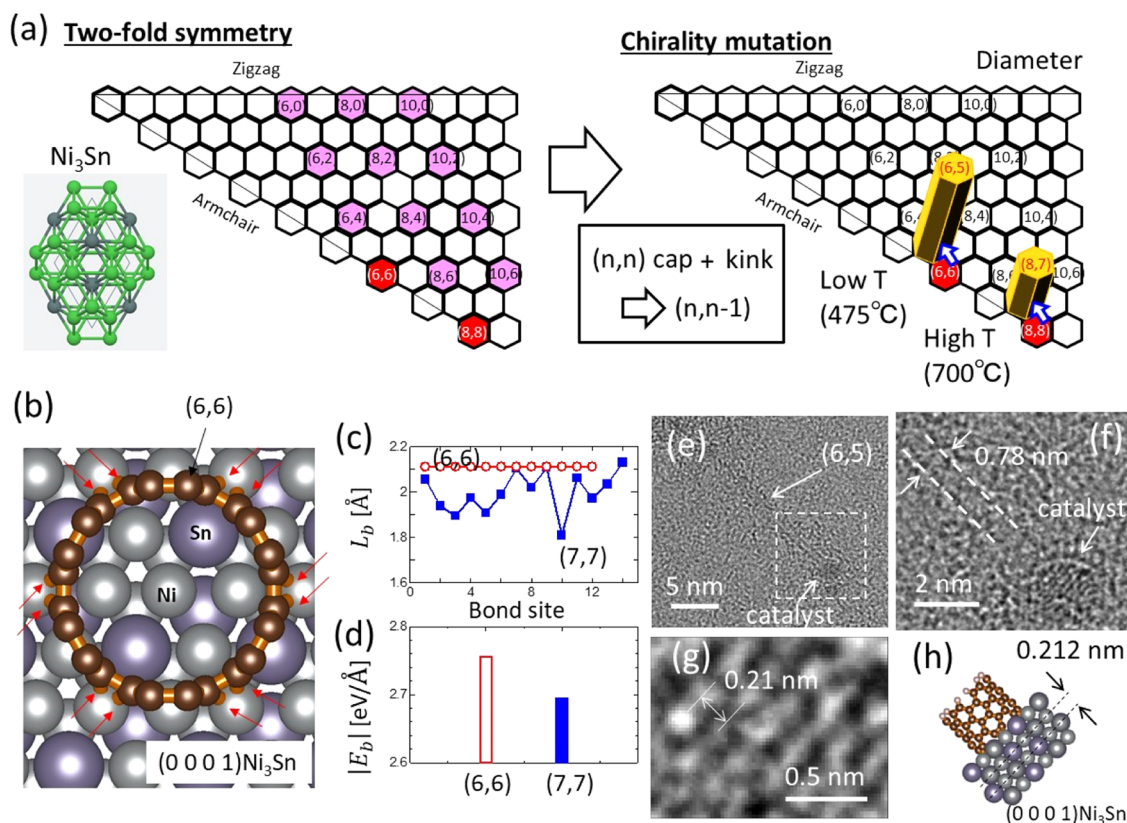
Figure 6. (a) Schematic illustration of twofold symmetry and chirality mutation. (b) Image of the stable structure of (6,6) CNT on (0001)Ni$_3$Sn. Arrows show locations of bonds between carbon and Ni. (c) Plot of each L_b between the edge of the carbon atom and the Ni$_3$Sn surface (○: (6,6) CNT and ■: (7,7) CNT), where binding energy becomes maximum for each chirality. (d) Maximum E_b for (6,6) and (7,7) CNTs on (0001)Ni$_3$Sn. (e) Low- and (f) high-magnification TEM images of (6,5) CNT with the catalyst nanoparticle. (g) Enlarged TEM image of the catalyst part in (f). (h) Side view of (0001)Ni$_3$Sn.

increase respectively, resulting in the increase in the E_a difference between (7,5) CNTs and (6,5) CNTs ($\Delta E_a = E_{a75} - E_{a65}$) to ~0.76 eV with P_{rt} (Figure 5c,d). This indicates that Ni$_3$Sn is formed during the P_{rt} process, increasing ΔE_a and resulting in the ultrahigh-purity synthesis of (6,5) CNTs. Furthermore, it was found that the addition of a small amount of water during the synthesis can further increase the ΔE_a to ~0.9 eV (Figure 5d). Purity is plotted vs Y for these modifications of the synthesis procedure, as shown in Figure 5e, indicating that ultrahigh purity (~95.8%) of (6,5) CNTs is achieved by decreasing the temperature to 475 °C with P_{rt} and adding a small amount of water during the synthesis.

Recently, it was proposed that the preferential growth of near armchair $(n,n-1)$ CNTs can be explained by the balance between the stability of cap formation and the growth rate, which are thermodynamically and kinetically determined factors, respectively.[4,23,24] (n,n) is known to have the highest nucleation probability and lowest growth rate because of the strong bonding between the SWNTs and the catalyst surface. Once kinks, such as a pentagon–heptagon pair, are introduced to (n,n), the chirality can change to $(n,n-1)$. As the growth rate of $(n,n-1)$ is faster than that of (n,n), $(n,n-1)$ can dominate within the as-grown sample.[4] Following this model, our result can be explained by (i) stable (6,6) CNT formation at Ni$_3$Sn due to symmetry matching, followed by (ii) selective mutation from (6,6) to (6,5) CNTs (Figure 6a). To validate this hypothesis, structural matching between (6,6) CNTs and Ni$_3$Sn was examined using density functional theory (DFT) calculations. Through the adjustment of the structure, it was

found that the twofold symmetry of (0001)Ni$_3$Sn is a special feature, where the standard deviation of the bond length (L_b) between the carbon edge of (6,6) CNTs and Ni (SDL$_{66}$) is 2.9 × 10^{-8} Å, much smaller than that of (7,7) CNTs (SDL$_{77}$ = 8.8 × 10^{-2} Å) (Figure 6b,c). The binding energy per unit length (E_b) of (6,6) CNTs on (0001)Ni$_3$Sn was 2.755 eV/Å, which was higher than that of (7,7) CNTs (2.694 eV/Å) (Figures 6d, S19, and S20). This indicates that the (6,6) CNT structure matches the specific position of (0001)Ni$_3$Sn well due to symmetry matching so that the nucleation of (6,6) CNTs is drastically enhanced compared to other chirality species.

The mutation may occur along several pathways from (n,n) to $(n,n-1)$, $(n,n-2)$, $(n+1,n)$, and $(n+1,n-1)$, with the rates for the pathways determined by the energy barriers for the introduction of the kinks for the mutation.[4] Because our synthesis was carried out at a very low growth temperature (475 °C), only limited mutations with the lowest energy barrier were allowed, namely, mutations to $(n,n-1)$.[4] It has been reported that the energy barrier difference between the smallest $(n,n-1)$ and second smallest $(n+1,n)$ mutations was approximately 1.07 eV,[4] which is close to the ΔE_a (~0.9 eV) measured in our experiments, indicating that ΔE_a may be related to the mutation energy barrier. This may also explain the selective mutation of (6,6) CNTs to (6,5) CNTs in our very low-temperature plasma processing.

Further direct evidence for the mutation to (6,5) CNTs was obtained by TEM measurements (see Methods for detailed information about sample preparation). A CNT with a diameter of 0.78 nm, which is consistent with (6,5) CNTs,
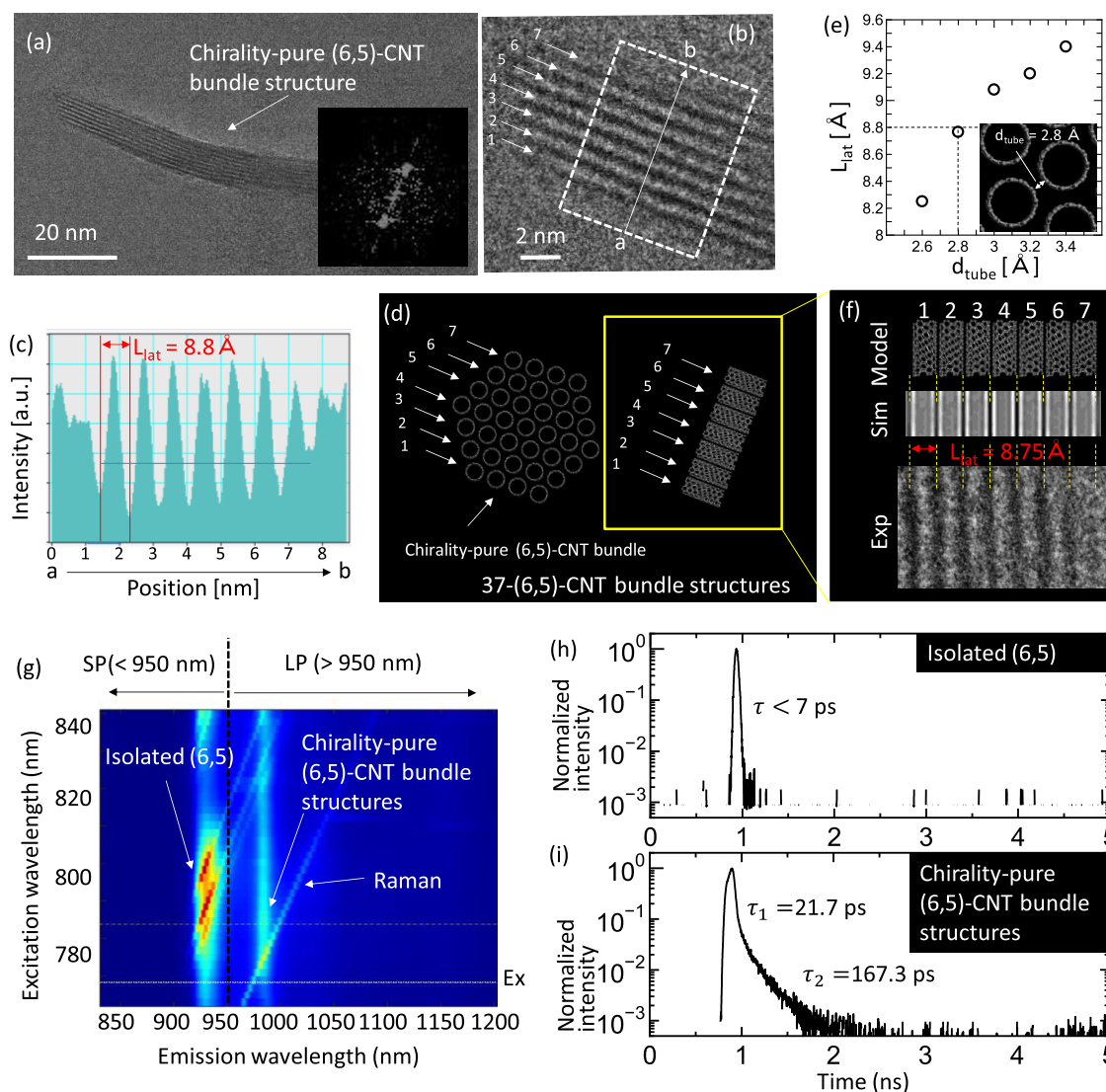
Figure 7. Chirality-pure (6,5)-CNT bundle structure formation and excitonic features. (a) Low- and (b) high-magnification TEM images of chirality-pure (6,5)-CNT bundle structures. The inset in (a) shows the FFT pattern of (b). (c) Integrated intensity of the contrast in the square region of (b) plotted from a to b. (d) Typical structure of 37-(6,5)-CNT bundle structures. (e) Calculated L_{lat} as a function of d_{tube}. (f) Structure comparison of the model, simulated TEM image (Sim), and experimental TEM image (Exp) of (6,5)-CNT bundle structures. (g) PLE mapping at longer excitation wavelength region measured for as-grown (6,5) CNT powder. PL lifetime of as-grown (6,5) CNT powder excited at 778 nm (EX) and collected with (h) short-pass (SP) filter (<950 nm) and (i) long-pass (LP) filter (>950 nm).

combined with a catalyst particle, can be identified from Figure 6e and its enlarged image (Figure 6f). The catalyst particle shows clear lattice fringes with an interplanar spacing of 0.21 nm, which is consistent with that of the (0001) plane of Ni_3Sn (0.212 nm) (Figure 6h), as observed in the enlarged image (Figure 6g) of Figure 6f. These results strongly support the validity of the DFT calculations.

As the symmetry matching of (6,6) CNTs and (0001)Ni_3Sn is critical, other twofold symmetry chiralities could also be grown under different conditions. Notably, when the growth temperature was increased to 700 °C, the dominant chirality increased from (6,5) CNTs to (8,7) CNTs, except for the (7,6) CNTs known as the nearest neighbor $(n,n-1)$ chirality of (6,5) CNTs (Figure S21). This can be explained by the enhanced nucleation of (8,8) CNTs (twofold symmetry) from Ni_3Sn, and the $(n,n-1)$ mutation giving rise to the preferential synthesis of (8,7) CNTs (Figure 6a). As the (7,7) CNTs cap does not have a twofold symmetry,

preferential growth of (7,6) CNTs could not be observed, supporting the accuracy of our explanation for the symmetry-driven (n,n) nucleation and $(n,n-1)$ mutation. The relatively broad chirality distribution of (8,7) CNTs compared to that of (6,5) CNTs may be due to the higher growth temperature causing further mutations $(n,n-1)$, $(n+1,n)$, $(n,n-1)$, and $(n+1,n-1)$.

An additional result supports the validity of this model. If small L_b is critical to the ultrahigh-purity synthesis of (6,5) CNTs, another catalyst possessing twofold symmetry with an atom size similar to Ni_3Sn should also be able to realize ultrahigh-purity (6,5) CNT growth. Next, we focused on Ni_3Sb, which is known to have a structure similar to that of Ni_3Sn. As expected, a similar purity of (6,5) CNTs (~87%) was obtained from the Ni + Sb (NiSb) catalyst (Figure S22), strongly supporting the importance of the small L_b with a twofold symmetry catalyst for (6,5) CNT growth. Note that

we did not measure the crystal structure of the Ni + Sb catalyst.

The above-described systematic experimental and computational results provide strong support for the validity of our explanation for the growth model of (6,5) CNTs, where selective nucleation of (6,6) CNTs occurs owing to the structural matching of (0001)Ni$_3$Sn followed by limited mutation to (6,5) CNTs due to the very low growth temperature in our plasma CVD. It is important to note that no (6,6) CNT signals were detected in experiments such as UV−vis−NIR and Raman spectra. This may be attributed to the relatively short length of (6,6) CNTs (approximately a few nanometers), which falls below the threshold for optical identification. As mentioned earlier, the growth rate of armchair nanotubes, such as (6,6) CNTs, is slow due to the stable armchair structure formed by all carbon atoms on the catalyst's surface. Defects introduced during growth can convert (6,6) CNTs to (6,5) CNTs. Since the growth rate of (6,5) CNTs is significantly faster than that of (6,6) CNTs, the CNTs reaching a length suitable for optical identification may primarily consist of (6,5) CNTs. It is possible that very short (6,6) CNTs or only cap structures of (6,6) CNTs remain on the surface of the NiSnFe catalyst, but experimental identification of these very short or cap structures is challenging.

Notably, our as-grown ultrahigh-purity (6,5) CNT solution dispersed in deuterium oxide (D$_2$O) + sodium cholate did not show a purple-like color of (6,5) CNTs, which can be explained by the strong background peak in the UV−vis−NIR spectra. The color of the SWNT solution is determined by the absorption spectra in the visible range of 380−770 nm. In this region, E22 absorption of (6,5) CNTs appears around 580 nm, corresponding to the yellow region. Therefore, transparent light passing through this solution should be a mixture of blue and red, resulting in a purple-like color for high-purity (6,5) CNTs. Upon closer examination of our high-purity (6,5) CNTs in this visible region (380−770 nm), only E22 absorption of (6,5) can be observed, similar to the chemically separated sample (Figure S5). However, the baseline is consistently much higher than that of (6,5) CNT absorption (Figure S5). Consequently, the solution appears to be dark gray. SEM measurements confirm the presence of byproducts, such as graphene flakes or carbon nanowall-like materials, on the surface of zeolite (Figure S23). These byproducts cause broad absorption in the 380−770 nm region, resulting in a black color in the solution. Interestingly, our as-grown (6,5) CNTs could be stably dissolved, even in deionized (DI) water, without any surfactant wrapping. The water solubility of (6,5) CNTs disappeared when the catalyst particles were removed via acid treatment (Figure S24). This indicates that the water solubility of the as-grown (6,5) CNTs is related to that of the catalyst particles (NiO/NiSn core−shell particles or NiSn nanoparticles) that are tightly bound to the short (6,5) CNTs. This stable water solubility of as-grown ultrahigh-purity (6,5) CNTs is highly important for bioimaging applications because it can decrease the total injection amount of SWNTs, resulting in reduced toxicity.

Synthesis and Excitonic Features of Chirality-Pure (6,5)-CNT Bundle Structures. Thin bundled CNTs were frequently observed in the TEM measurements; such CNTs should be naturally formed during the dispersion process for TEM sample preparation (Figure 7a). Interestingly, the individual CNTs within the bundle are well-aligned and form

a periodic lattice with a lattice parameter of 8.8 Å (L_{lat}) (Figure 7b,c), which is attributed to the very high original (6,5) CNT purity (>90%) and surfactant-free clean surface. Since 7 lines and spaces are clearly observed in the TEM image (Figure 7a), this bundle structure can be assumed to be formed by 37 (6,5) CNTs and is named 37-(6,5)-CNT bundle structures (Figure 7d). To identify the detailed bundle structure, L_{lat} was calculated with simulated TEM by changing the tube-to-tube distance (d_{tube}) of the 37-(6,5)-CNT bundle structures (Figure 7e). It was found that d_{tube} = 2.8 Å for L_{lat} matched the experimental data (8.8 Å) (Figure 7c,e). For this structure, the simulated TEM image of the 37-(6,5)-CNT bundle structures matches the experimental TEM image well (Figure 7f). While the diameter appears uniform within the bundle structures, the diffraction spot obtained from the FFT was not as sharp as anticipated for the bundle structures (inset in Figure 7a). This lack of sharpness may be attributed to the imperfect control of tube-to-tube distance, possibly influenced by strain issues or small amounts of impurities. These aspects need to be further explored and discussed in future studies.

Interestingly, our high-purity (6,5) CNTs show clear PL even in the as-grown powder form (Figure S25a). This can be explained by the zeolite powder used for catalyst support materials, which can enhance the formation of the freestanding shape of isolated (6,5) CNTs that prevents exciton quenching through the substrate (Figure S25b). PLE mapping shows two clear spots (P$_A$ and P$_B$) (Figure S25a). The air-suspended CNTs are known to exhibit a blue shift in both excitation and emission wavelengths compared to samples dispersed in solution.[25,26] Taking this environmental effect into account, P$_A$ can be identified as the peak originating from the (6,5) CNTs. To identify the origin of P$_B$, a small amount of ethanol was added dropwise, and the sample was dried. Then, P$_A$ disappeared, and an additional peak P$_C$, slightly red-shifted compared to P$_B$, appeared (Figure S25c). It is known that bundle formation can be enhanced by dropwise addition and drying of liquid to the as-grown CNTs,[27] i.e., P$_B$ and P$_C$ can be attributed to bundled (6,5) CNTs (Figure S25d). The difference between P$_B$ and P$_C$ can be explained by the redshift with increasing bundle size due to environmental effects.[28] Therefore, we can conclude that P$_B$ and P$_C$ are due to bundled (6,5) CNTs. Since our initial sample contains (6,5) CNTs with a purity of more than 90% and has a surfactant-free clean surface, this bundle consists of only (6,5) CNTs with well-crystallized structures as demonstrated by TEM analysis (Figure 7a−f), indicating that P$_B$ and P$_C$ are due to PL from chirality-pure (6,5)-CNT bundle structures.

PL lifetime (τ) measurements were carried out for P$_A$ (isolated (6,5) CNTs) and P$_B$ (chirality-pure (6,5)-CNTs bundle structures) in the same sample (Figure 7g). Note that this measurement was conducted using wavelength-tunable Ti:sapphire laser excitation. Due to the wavelength range of the measurement system used being in the near-infrared, measurements were performed not with the conventional E22 excitation (450−750 nm, Figure S25a,c) but with the K-momentum phonon sideband of the dark exciton of E11 (770−840 nm, Figure 7g) (see the Methods section for more detailed information). Although τ for isolated (6,5) CNTs (P$_A$) is below the time resolution of the detector, we estimate it to be less than 7 ps from reconvolution fitting using the instrument response function (Figure 7h). Interestingly, the lifetime of chirality-pure (6,5)-CNT bundle structures (P$_B$) shows biexponential decay with τ_1 = 21.7 ps and τ_2 = 167.3 ps

and is more than 20 times longer than that of the isolated (6,5) CNTs with single exponential decay (Figure 7i). This is an intrinsic feature of chirality-pure (6,5)-CNT bundle structures that can be explained by exciton delocalizations or intertube excitons. To the best of our knowledge, the exciton dynamics of chirality-pure CNT bundle structures have not been reported thus far. While there is a report in the literature discussing the intertube excitons with Raman scattering spectra, it does not report on PL features related to exciton dynamics.[29] Detailed excitonic features in chirality-pure CNT bundle structures will be elucidated further in future work.

The density of closely packed CNTs formed in our study is approximately 1.2×10^6 μm^2 (Figure 7a,b,d), which is higher than that fabricated by the post-treatment process (3.8×10^5 μm^2).[30] This is attributed to the smaller diameter of the CNTs and the closer intertube distance (2.8 Å) compared to the conventional interlayer distance of graphene of 3.4 Å. Since a stronger hybridization of the electron wave function can be expected for such a short intertube distance, additional unique electronic and optical properties can be expected to be observed for our directly fabricated chirality-pure CNT bundle structures.

It is important to highlight that our developed CNT growth method enables the ultrahigh-purity synthesis of (6,5) CNTs. However, the purity discussed in this study specifically refers to the ratio of (6,5) CNTs to other chirality CNTs. It is worth noting that several carbon-based byproducts can still be grown as impurities, as illustrated in Figure S23. While the optical measurements provide sufficient insight into the synthesis quantity, from an application perspective, there is a need to further develop it for mass production. In this regard, we believe that catalytic control techniques, selectively forming phase pure Ni_3Sn nanoparticle (<5 nm), which currently only partially exists, are crucial. Enhancing the growth yield of (6,5) CNTs and minimizing the production of such byproducts will be the focus of our future investigations.

CONCLUSIONS

We realized an ultrahigh-purity synthesis of (6,5) CNTs with the highest purity of up to 95.8%, using the trimetal catalyst NiSnFe. Ni_3Sn crystals were found to be the critical element causing the selective synthesis of (6,5), with Fe strongly enhancing the formation of Ni_3Sn. The chirality mutation from (n,n) to $(n,n-1)$ during plasma CVD at very low growth temperature (~475 °C), together with the twofold symmetry of Ni_3Sn, can be a possible explanation for the near-single-chirality synthesis of (6,5) SWNTs from the NiSnFe catalyst. As there are many possibilities for catalyst combinations, our finding, i.e., the importance of trimetallic catalysts for single-chirality synthesis, creates the huge possibility of realizing the on-demand synthesis of various single-chirality SWNTs. Detailed TEM analysis revealed that 37-(6,5)-CNT bundle structures are directly formed with closely packed structure (d_{tube} = 2.8 Å) by forming a thin bundle of ultrahigh-purity as-grown (6,5) CNTs. Furthermore, the directly synthesized chirality-pure (6,5)-CNT bundle structures show a PL lifetime that is more than 20 times longer than that of the isolated (6,5) CNTs, which can be explained by either exciton delocalization or intertube excitons.

METHODS

Catalyst Preparation. Zeolite-supported metal catalysts were prepared as follows. Initially, 0.5 wt % acetate tetrahydrate (and 0.5 wt

% acetate dimer) was mixed with ferrierite zeolite (typically 1 g). The prepared solid catalyst was then dissolved in 20 mL of ethanol and ultrasonicated for 15 min. After dispersion, the catalyst was heated under atmospheric conditions (80 °C, 24 h). The bimetallic and trimetallic catalysts were also prepared with a similar method. Each acetate solid powder, measured at 0.5 wt %, was first dissolved in ethanol. Zeolite was then added, and the mixture was subjected to ultrasonic dispersion followed by drying for 24 h.

Plasma CVD. A homemade plasma CVD system was used for diffusion plasma CVD.[12] Before plasma CVD growth was performed, an electric furnace was heated to the desired temperature (typically around 475−550 °C). After the desired temperature was reached, a CH_4 flow of 20 sccm (32 Pa) was employed. The catalyst holder was immediately transferred to the central area and subjected to rapid heating. When the catalyst holder was heated to the growth temperature, the pressure was adjusted to 60 Pa. Radio frequency of 28 W power (13.56 MHz) was supplied to the coils outside the quartz tube. A plasma irradiation time of 2 min was used. After plasma CVD, the CH_4 gas supply was stopped, and the substrate was removed from the electrical furnace to cool down.

Structural Characterizations. The chirality of the SWNTs was evaluated using a PLE map (NanoLog, Horiba, Japan), UV−vis−NIR spectroscopy (V-7200HK, JASCO, Japan), and Raman scattering spectroscopy (J/Y, HR800) with a semiconductor laser (532 nm), He−Cd laser (442 nm), He−Ne laser (633 nm), and semiconductor laser (785 nm). The crystalline structures of the catalysts and CNTs were confirmed using TEM (JEM-ARM200FC, equipped with a C_s corrector and operated at 120 kV), high-angle annular dark field (HAADF) and annular bright field (ABF)-STEM (JEOL, JEM-ARM200F), STEM-EDX (JEOL, JED-2300), XANES and EXAFS (High Energy Accelerator Research Organization, Photon Factory, Japan, measured by Toray Research Center, Inc.), and XRD (measured by Toray Research Center, Inc.). The XRD spectra shown in Figure 3d−f display only the catalyst component information obtained by measuring the spectra of the zeolite-supported catalysts and the zeolite alone separately and then subtracting the latter from the former (Figure S26).

Estimation of Chirality Purity of CNTs. The purity of CNTs was estimated with a PLE map, UV−vis−NIR spectroscopy, and Raman scattering spectroscopy. The detailed estimation methods using each approach are as follows:

PLE map: For samples with >90% (6,5) CNTs, mainly (6,5) and (7,5) CNT peaks are observed with a slight presence of the (6,4) CNT peak (Figure S4). Accordingly, we extracted spectra of the excitation energy dependence of the emission intensity for each chirality corresponding to the emission wavelengths with the highest emission intensity ((6,4) CNTs: 873.5 nm, (6,5) CNTs: 971.9 nm, (7,5) CNTs: 1016.4 nm). Each spectrum is then fitted by using a Lorentz function to calculate the integrated intensity of the fitting component for each chirality. We use the ratio of this integrated intensity as the chirality purity calculated from PLE. To obtain the accurate value of the highest (6,5) CNT purity, we also considered the effect of chirality-dependent PL quantum efficiencies. The PL quantum efficiencies of (6,5) and (6,4) CNT are 1.4 times and 1.5 times higher than that of (7,5) CNT, respectively.[31,32] As a result, we found that the purity of (6,5) CNTs, which was calculated as 97% from PLE alone, becomes 95.2% when considering the PL quantum efficiency. Regarding the chirality dependence of the PL quantum efficiency, due to remaining uncertainties or ambiguities regarding certain chiralities, in this study, the PL quantum efficiency was considered only when evaluating the absolute value of the highest (6,5) CNT purity.

UV−vis−NIR: First, the spectrum of 700−1250 nm, where many chiralities' E11 peaks exist, is extracted, and the background curve is determined by fitting with an exponential function (green line in Figure S5c). Subsequently, the spectrum shown in Figure 2e of the paper is obtained by subtracting the background curve obtained from fitting the original spectrum (red line in Figure S5c). Then, the component area ratios of (6,5), (7,5), and (6,4) CNTs are calculated by fitting analysis to determine purity (Table S2). Note that due to

the wavelength switching of the measurement system, there are discontinuities in the data at 850 and 1200 nm, so we are correcting this.

Raman scattering spectra: The as-grown SWNTs were characterized by using Raman spectroscopy with different excitation lasers (442, 532, 633, and 785 nm). Raman mapping was performed for the same samples to quantify the percentage of SWNTs with specific chirality by counting the number of RBMs. The Raman measurements were performed 886 times for (442, 532, 633 nm) and 234 times for a 785 nm excitation laser. Identifying chirality from the peak position of the RBM and calculating the abundance based on the occurrence probability of each chirality (Table S3 and Figure S6).

Sample Preparations. The as-grown CNTs were dispersed in deuterium oxide (D_2O) solution with sodium cholate (0.5 wt %) by needle-type ultrasonication for 1 h. The solution was then centrifuged at 30,000g for 3 h to obtain the SWNTs supernatant liquid used for PLE mapping and UV−vis−NIR measurements. The as-grown SWNT powder with zeolite was used for Raman, XANES, XRD, STEM, and EDX measurements. The SWNT solution was dropped onto TEM grids coated with a very thin (4 nm) carbon film (hyper-high-resolution carbon film, HHR-M05, STEM), followed by ultrasonication (1 h) and centrifugation (50,000g, 3 h) to remove the zeolite.

Device Fabrication and Measurements. Conventional electron beam lithography (Elionix, ELS-7500), vacuum evaporation of metal, and lift-off were used to fabricate the FET devices. The device performance was measured at room temperature by using a vacuum probe station with a semiconductor parameter analyzer (HP 4155C).

DFT Calculations. Electronic structure calculations were performed within the generalized gradient approximation (GGA)[33] using the Vienna Ab initio Simulation Package (VASP).[34,35] Projector-augmented-wave (PAW)[36] type pseudopotentials with a cutoff energy of 400 eV were employed. To calculate the energy of the SWNT on the $Ni_3Sn(0001)$ surface, $E_{SWNT-(0001)}$, a four-atomic-layered slab model with 3×3 periodicity in a hexagonal supercell with $a = 15.885$ Å and $c = 30$ Å, was used (Figure S19). The armchair SWNT was three times the length of the unit cell, and one side was terminated with hydrogen atoms. For Brillouin zone integration, only the Γ point was used. The binding energy per unit length was calculated as $E_b = (E_{SWNT-(0001)} - E_{SWNT} - E_{(0001)})/d$, where d is the diameter of the SWNT, and E_{SWNT} and $E_{(0001)}$ are the energies of the SWNT and $Ni_3Sn(0001)$ surfaces, respectively, calculated in the same supercell. To search for a stable geometry, we focused on the standard deviation of the shortest distances between the carbon atoms at the edge of the SWNT and the surface atoms. By fixing the geometry within the SWNT, that within the Ni_3Sn surface, and the distance between them, and only changing the in-plane relative position and angle, we obtained local minima of the standard deviation and their geometries. Next, by changing the distance between the SWNT and the Ni_3Sn surface, we calculated the lowest binding energy for each local minimum (Figure S20).

Exciton Lifetime Measurement. A home-built sample-scanning confocal microscopy system[26] is used for the PLE and time-resolved PL measurements shown in 7Figure 7g−i. We use a wavelength-tunable Ti:sapphire laser for excitation where the output can be switched between continuous wave (cw) and ∼100 fs pulses with a repetition rate of 76 MHz. The excitation laser beam passes through a shutter used for background subtraction and is focused onto the surface of the samples with a spot size of ∼1 μm with an objective lens with a numerical aperture of 0.85 and a focal length of 1.8 mm. The luminescence is collected by the same lens and is separated from the excitation laser with a dichroic beam splitter, which has a cut-on wavelength at 900 nm. For the PLE measurements, continuous-wave excitation at a power of 1 mW is used. The PL spectra are measured with a liquid-nitrogen-cooled 512-pixel linear InGaAs photodiode array attached to a 300 mm spectrometer with a 150 lines/mm grating blazed at 1.25 μm, and an integration time of 2 s is used. The time-resolved PL measurements are performed by using a fiber-coupled superconducting single-photon detector and a time-correlated single-photon counting module. Pulsed excitation with a wavelength of 778

nm and an average excitation power of 5 μW is used. A short-pass filter with a cutoff wavelength at 950 nm and a long-pass filter with a cut-on wavelength at 950 nm are used as shown in Figure 7h,i, respectively. The data in Figure 7h,i are fit with a single exponential function and a biexponential function, convoluted with the instrument response function. All measurements are performed at room temperature in air.

ASSOCIATED CONTENT

ⓢ Supporting Information

The Supporting Information is available free of charge at https://pubs.acs.org/doi/10.1021/acsnano.4c01475.

Summary of catalysts and purity of various CNTs (Table S1); fitted and calculated relative abundance of different (n,m) in 475 °C sample from UV−vis−NIR spectra (Table S2); statistics on the RBM peaks and the corresponding (n,m) for the sample grown at 475 °C (Table S3); possible combination of bimetal catalysts (Figure S1); PLE maps of SWNTs grown at 550 °C without P_{rt} using various combinations of bimetal catalysts (Figure S2); PLE maps of SWNTs grown at 550 °C without P_{rt} using various combinations of trimetal catalysts (Figure S3); schematic diagram outlining the method for calculating chirality purity from the PLE map (Figure S4); raw and full-range UV−vis−NIR spectra of ultrahigh and low-purity (6,5) CNTs grown with the NiSnFe catalyst at 475 °C with P_{rt} and 650 °C without P_{rt} (Figure S5); Kataura plot and raw RBM spectra of ultrahigh-purity (6,5) CNTs grown at 475 °C with P_{rt} measured by different laser excitations: 785, 633, 532, 442 nm (Figure S6); typical TEM images of (6,5) CNTs grown from the NiSnFe catalyst (Figure S7); typical electrical transport properties of FET with ultrahigh-purity (6,5) CNTs (Figure S8); typical EXAFS measurements of FT-magnitude radial distance dependence for Ni, NiSn, and NiSnFe catalysts (Figure S9); typical TEM images of the core−shell structure of the NiSnFe nanoparticles (Figure S10); structural identification of Ni and Ni_3Sn with STEM images and FFT patterns for relatively large (>5 nm) NiSnFe nanoparticles (Figures S11 and S12); typical STEM image of NiSnFe nanoparticle, where thickness of the NiO shell is varied according to the core structures (Figure S13); typical STEM images and element mapping of small (<5 nm) NiSnFe nanoparticles (Figures S15 and S16); plot of (6,5) CNT purity vs absolute PL intensity of (6,5) CNTs grown using different combinations of NiSnFe ratios grown at 550 °C without P_{rt} (Figure S17); typical XRD spectra of NiSnFe treated by different pretreatment temperatures (Figure S18); top and side view of the slab model used in the present study (Figure S19); binding energy per unit length, E_b, as a function of the standard deviation of the bond lengths between edge carbon atoms and surface atoms, σ_r (Figure S20); temperature dependence of the (6,5), (7,6), and (8,7) CNT purities (Figure S21); schematic illustration of crystal structures of Ni_3Sn and Ni_3Sb (Figure S22); typical (a) low, (b) middle, and (c) high-magnification SEM images of the zeolite surface after the growth of (6,5) CNTs (Figure S23); water solubility of the as-grown ultrahigh-purity (6,5) CNTs; PLE measurements for as-grown (6,5) CNTs with zeolite powder (Figure

S25); and raw XRD spectra of NiSnFe/zeolite, NiSn/zeolite, Ni/zeolite, and zeolite only (Figure S26) (PDF)

AUTHOR INFORMATION

Corresponding Author

Toshiaki Kato − *Graduate School of Engineering, Tohoku University, 980-8579 Sendai, Japan; Advanced Institute for Materials Research (AIMR), Tohoku University, 980-8577 Sendai, Japan;* orcid.org/0000-0003-1010-7357; Email: kato12@tohoku.ac.jp

Authors

Satoru Shiina − *Graduate School of Engineering, Tohoku University, 980-8579 Sendai, Japan; Advanced Institute for Materials Research (AIMR), Tohoku University, 980-8577 Sendai, Japan*

Tennpei Murohashi − *Graduate School of Engineering, Tohoku University, 980-8579 Sendai, Japan; Advanced Institute for Materials Research (AIMR), Tohoku University, 980-8577 Sendai, Japan*

Koyo Ishibashi − *Graduate School of Engineering, Tohoku University, 980-8579 Sendai, Japan; Advanced Institute for Materials Research (AIMR), Tohoku University, 980-8577 Sendai, Japan*

Xing He − *Graduate School of Engineering, Tohoku University, 980-8579 Sendai, Japan; Advanced Institute for Materials Research (AIMR), Tohoku University, 980-8577 Sendai, Japan*

Takashi Koretsune − *Department of Physics, Tohoku University, 980-8578 Sendai, Japan*

Zheng Liu − *Innovative Functional Materials Research Institute, National Institute of Advanced Industrial Science and Technology (AIST), 463-8560 Nagoya, Japan;* orcid.org/0000-0001-9095-7647

Wataru Terashima − *Nanoscale Quantum Photonics Laboratory, RIKEN Cluster for Pioneering Research, 351-0198 Wako, Japan*

Yuichiro K. Kato − *Nanoscale Quantum Photonics Laboratory, RIKEN Cluster for Pioneering Research, 351-0198 Wako, Japan; Quantum Optoelectronics Research Team, RIKEN Center for Advanced Photonics, 351-0198 Wako, Japan;* orcid.org/0000-0002-9942-1459

Kazutoshi Inoue − *Advanced Institute for Materials Research (AIMR), Tohoku University, 980-8577 Sendai, Japan*

Mitsuhiro Saito − *Institute of Engineering Innovation, School of Engineering, The University of Tokyo, 113-8656 Tokyo, Japan;* orcid.org/0000-0003-1602-0308

Yuichi Ikuhara − *Advanced Institute for Materials Research (AIMR), Tohoku University, 980-8577 Sendai, Japan; Institute of Engineering Innovation, School of Engineering, The University of Tokyo, 113-8656 Tokyo, Japan; Nanostructures Research Laboratory, Japan Fine Ceramics Center, 456-8587 Nagoya, Japan;* orcid.org/0000-0003-3886-005X

Complete contact information is available at:
https://pubs.acs.org/10.1021/acsnano.4c01475

Author Contributions

◆S.S. and T.M. authors contributed equally to this work. This manuscript was written through contributions of all authors. All authors have given approval to the final version of the manuscript.

Notes

The authors declare no competing financial interest.

REFERENCES

(1) Yang, F.; Wang, X.; Si, J.; Zhao, X.; Qi, K.; Jin, C.; et al. Water-assisted preparation of high-purity semiconducting (14, 4) carbon naotubes. *ACS Nano* **2017**, *11*, 186−193.

(2) Yang, F.; Wang, X.; Zhang, D.; Yang, J.; Luo, D.; Xu, Z.; Wei, J.; Wang, J.-Q.; Xu, Z.; Peng, F.; Li, X.; Li, R.; Li, Y.; Li, M.; Bai, X.; Ding, F.; Li, Y. Chirality-specific growth of single-walled carbon nanotubes on solid alloy catalysts. *Nature* **2014**, *510*, 522−524.

(3) Zhang, S.; Kang, L.; Wang, X.; Tong, L.; Yang, L.; Wang, Z.; Qi, K.; Deng, S.; Li, Q.; Bai, X.; Ding, F.; Zhang, J. Arrays of horizontal carbon nanotubes of controlled chirality grown using designed catalysts. *Nature* **2017**, *543*, 234−238.

(4) Zhang, S.; Wang, X.; Yao, F.; He, M.; Lin, D.; Ma, H.; Sun, Y.; Zhao, Q.; Liu, K.; Ding, F.; Zhang, J. Controllable Growth of (n, n −1) Family of Semiconducting Carbon Nanotubes. *Chem* **2019**, *5*, 1182−1193.

(5) Yang, F.; Wang, X.; Zhang, D.; Qi, K.; Yang, J.; Xu, Z.; Li, M.; Zhao, X.; Bai, X.; Li, Y. Growing Zigzag (16,0) Carbon Nanotubes with Structure-Defined Catalysts. *J. Am. Chem. Soc.* **2015**, *137*, 8688−8691.

(6) An, H.; Kumamoto, A.; Takezaki, H.; Ohyama, S.; Qian, Y.; Inoue, T.; Ikuhara, Y.; Chiashi, S.; Xiang, R.; Maruyama, S. Chirality specific and spatially uniform synthesis of single-walled carbon nanotubes from a sputtered Co−W bimetallic catalyst. *Nanoscale* **2016**, *8*, 14523−14529.

(7) Wang, H.; Wang, B.; Quek, X.-Y.; Wei, L.; Zhao, J.; Li, L.-J.; Chan-Park, M. B.; Yang, Y.; Chen, Y. Selective Synthesis of (9,8) Single Walled Carbon Nanotubes on Cobalt Incorporated TUD-1 Catalysts. *J. Am. Chem. Soc.* **2010**, *132*, 16747−16749.

(8) He, M.; Jiang, H.; Liu, B.; Fedotov, P. V.; Chernov, A. I.; Obraztsova, E. D.; Cavalca, F.; Wagner, J. B.; Hansen, T. W.; Anoshkin, I. V.; Obraztsova, E. A.; Belkin, A. V.; Sairanen, E.; Nasibulin, A. G.; Lehtonen, J.; Kauppinen, E. I. Chiral-Selective Growth of Single-Walled Carbon Nanotubes on Lattice-Mismatched Epitaxial Cobalt Nanoparticles. *Sci. Rep.* **2013**, *3*, No. 1460.

(9) He, M.; Chernov, A. I.; Fedotov, P. V.; Obraztsova, E. D.; Sainio, J.; Rikkinen, E.; Jiang, H.; Zhu, Z.; Tian, Y.; Kauppinen, E. I.; Niemela, M.; Krause, A. O. I. Predominant (6,5) Single-Walled Carbon Nanotube Growth on a Copper-Promoted Iron Catalyst. *J. Am. Chem. Soc.* **2010**, *132*, 13994−13996.

(10) Li, X.; Tu, X.; Zaric, S.; Welsher, K.; Seo, W. S.; Zhao, W.; Dai, H. Selective Synthesis Combined with Chemical Separation of Single-Walled Carbon Nanotubes for Chirality Selection. *J. Am. Chem. Soc.* **2007**, *129*, 15770−15771.

(11) Lolli, G.; Zhang, L.; Balzano, L.; Sakulchaicharoen, N.; Tan, Y.; Resasco, D. E. Tailoring (n,m) Structure of Single-Walled Carbon Nanotubes by Modifying Reaction Conditions and the Nature of the Support of CoMo Catalysts. *J. Phys. Chem. B* **2006**, *110*, 2108−2115.

(12) Xu, B.; Kaneko, T.; Shibuta, Y.; Kato, T. Preferential synthesis of (6,4) single-walled carbon nanotubes by controlling oxidation degree of Co catalyst. *Sci. Rep.* **2017**, *7*, No. 11149.

(13) He, M.; Wang, X.; Zhang, L.; Wu, Q.; Song, X.; Chernov, A. I.; Fedotov, P. V.; Obraztsova, E. D.; Sainio, J.; Jiang, H.; Cui, H.; Ding, F.; Kauppinen, E. Anchoring effect of Ni^{2+} in stabilizing reduced metallic particles for growing single-walled carbon nanotubes. *Carbon* **2018**, *128*, 249−256.

(14) Yang, F.; Wang, M.; Zhang, D.; Yang, J.; Zheng, M.; Li, Y. Chirality Pure Carbon Nanotubes: Growth, Sorting, and Characterization. *Chem. Rev.* **2020**, *120*, 2693−2758.

(15) Wallace, W. E.; Karlicek, R. F.; Imamura, H. Mechanism of hydrogen absorption by $LaNi_5$. *J. Phys. Chem. A* **1979**, *83*, 1708−1712.

(16) Nagamatsu, J.; Nakagawa, N.; Muranaka, T.; Zenitani, Y.; Akimitsu, J. Superconductivity at 39K in magnesium diboride. *Nature* **2001**, *410*, 63−64.

(17) Kahn, H.; Huff, M. A.; Heuer, A. H. The TiNi shape-memory alloy and its applications for MEMS. *J. Micromech. Microeng.* **1998**, *8*, 213−221.

(18) Studt, F.; Sharafutdinov, I.; Abild-Pedersen, F.; Elkjær, C. F.; Hummelshøj, J. S.; Dahl, S.; Chorkendorff, I.; Nørskov, J. K. Discovery of a Ni-Ga catalyst for carbon dioxide reduction to methanol. *Nat. Chem.* **2014**, *6*, 320−324.

(19) Liu, H.; Nishide, D.; Tanaka, T.; Kataura, H. Large-scale single-chirality separation of single-wall carbon nanotubes by simple gel chromatography. *Nat. Commun.* **2011**, *2*, No. 309.

(20) Kim, W.; Javey, A.; Tu, R.; Cao, J.; Wang, Q.; Dai, H. Electrical contacts to carbon nanotubes down to 1 nm in diameter. *Appl. Phys. Lett.* **2005**, *87*, No. 173101.

(21) Darby, B. L.; Yates, B. R.; Martin-Bragado, I.; Gomez-Selles, J. L.; Elliman, R. G.; Jones, K. S. Substrate orientation dependence on the solid phase epitaxial growth rate of Ge. *J. Appl. Phys.* **2013**, *113*, No. 033505.

(22) Saito, M.; Li, H.; Inoue, K.; Matsuhata, H.; Ikuhara, Y. Oxygen atom ordering on SiO_2 /4H-SiC {0 0 01} polar interfaces formed by wet oxidation. *Acta Mater.* **2021**, *221*, No. 117360.

(23) Artyukhov, V. I.; Penev, E. S.; Yakobson, B. I. Why nanotubes grow chiral. *Nat. Commun.* **2014**, *5*, No. 4892.

(24) Wang, X.; Ding, F. How a Solid Catalyst Determines the Chirality of the Single-Wall Carbon Nanotube Grown on It. *J. Phys. Chem. Lett.* **2019**, *10*, 735−741.

(25) Kiowski, O.; Lebedkin, S.; Hennrich, F.; Malik, S.; Rösner, H.; Arnold, K.; Sürgers, C.; Kappes, M. M. Photoluminescence microscopy of carbon nanotubes grown by chemical vapor deposition: Influence of external dielectric screening on optical transition energies. *Phys. Rev. B* **2007**, *75*, No. 075421, DOI: 10.1103/PhysRevB.75.075421.

(26) Ishii, A.; Yoshida, M.; Kato, Y. K. Exciton diffusion, end quenching, and exciton-exciton annihilation in individual air-suspended carbon nanotubes. *Phys. Rev. B* **2015**, *91*, No. 125427, DOI: 10.1103/PhysRevB.91.125427.

(27) Futaba, D. N.; Hata, K.; Yamada, T.; Hiraoka, T.; Hayamizu, Y.; Kakudate, Y.; Tanaike, O.; Hatori, H.; Yumura, M.; Iijima, S. Shape-engineerable and highly densely packed single-walled carbon nanotubes and their application as super-capacitor electrodes. *Nat. Mater.* **2006**, *5*, 987−994.

(28) Tan, P. H.; Hasan, T.; Bonaccorso, F.; Scardaci, V.; Rozhin, A. G.; Milne, W. I.; Ferrari, A. C. Optical properties of nanotube bundles by photoluminescence excitation and absorption spectroscopy. *Phys. E* **2008**, *40*, 2352−2359.

(29) Simpson, J. R.; Roslyak, O.; Duque, J. G.; Hároz, E. H.; Crochet, J. J.; Telg, H.; Piryatinski, A.; Walker, A. R. H.; Doorn, S. K. Resonance Raman signature of intertube excitons in compositionally-defined carbon nanotube bundles. *Nat. Commun.* **2018**, *9*, No. 637.

(30) Gao, W.; Kono, J. Science and applications of wafer-scale crystalline carbon nanotube films prepared through controlled vacuum filtration. *R. Soc. Open Sci.* **2019**, *6*, No. 181605.

(31) Wei, X.; Tanaka, T.; Li, S.; Tsuzuki, M.; Wang, G.; Yao, Z.; Li, L.; Yomogida, Y.; Hirano, A.; Liu, H.; Kataura, H. Photoluminescence Quantum Yield of Single-Wall Carbon Nanotubes Corrected for the Photon Reabsorption Effect. *Nano Lett.* **2020**, *20*, 410−417.

(32) Carlson, L. J.; Maccagnano, S. E.; Zheng, M.; Silcox, J.; Krauss, T. D. Fluorescence Efficiency of Individual Carbon Nanotubes. *Nano Lett.* **2007**, *7*, 3698−3703.

(33) Perdew, J. P.; Burke, K.; Ernzerhof, M. Generalized gradient approximation made simple. *Phys. Rev. Lett.* **1996**, *77*, No. 3865.

(34) Kresse, G.; Furthmüller, J. Efficient iterative schemes for ab initio total-energy calculations using a plane-wave basis set. *Phys. Rev. B* **1996**, *54*, No. 11169.

(35) Kresse, G.; Furthmüller, J. Efficiency of ab-initio total energy calculations for metals and semiconductors using a plane-wave basis set. *Comput. Mater. Sci.* **1996**, *6*, 15.

(36) Blöchl, P. E. Projector augmented-wave method. *Phys. Rev. B: Condens. Matter Mater. Phys.* **1994**, *50*, No. 17953.